Eur. Phys. J. D (2025) 79:74
https://doi.org/10.1140/epjd/s10053-025-01025-7

THE EUROPEAN
PHYSICAL JOURNAL D

Regular Article - Nonlinear Dynamics

Out-of-Time-Order Correlation in perturbed quantum wells

Pranaya Pratik Das[1,a] and Biplab Ganguli[1,b]

[1] Department of Physics and Astronomy, National Institute of Technology Rourkela, Odisha 769008, India

Received 19 December 2024 / Accepted 10 June 2025 / Published online 28 June 2025

Abstract. *Out-of-Time-Order Correlator* (OTOC) and *Loschmidt Echo* (LE) are commonly regarded as diagnostic tools for chaos, although they may yield misleading results, as we observe. Previous studies have concluded that OTOC shows exponential growth in the neighbourhood of a local maximum. If this statement holds true, the exponential growth should break off once the local maximum is no longer present within the system. By applying a small symmetry-breaking perturbation, we notice that the behaviour of the OTOCs remains remarkably resilient even in the absence of a maximum. Besides this, we also notice that with the increase in perturbation strength, the broken symmetric region expands, causing a broader range of eigenstates to engage in the exponential growth of OTOCs. Therefore, the critical factor lies not in the presence of a local maximum, but in the dynamic nature of the density of states in the broken symmetry regions. Our examination, spanning diverse one- dimensional potential landscapes, reveals the universality of this phenomenon. We also use other chaos diagnostic tool, LE. Interestingly, it also gives a false signal of chaos.

1 Introduction

The Lyapunov exponent, extensively discussed in notable publications[1–4], effectively characterises classical chaos. It measures the divergence of nearby trajectories in phase space, which is a measure of sensitivity to initial conditions. However, the Heisenberg uncertainty principle dictates that, for a system with N degrees of freedom, a single quantum state occupies a volume of $\hbar^N$ in classical phase space. Hence, we no longer have the luxury of following individual orbits. Thus, there is a pressing need for a chaos diagnostic tool tailored for quantum systems.

Several diagnostic tools are developed over the years to detect chaos in quantum systems. Some of them are level spacing distribution [5,6], *Spectral Form Factor* (SFF) [7–9], level number variance [8–10], entanglement power [11–14], quantum coherence [15], LE [16–20], etc. Nonetheless, the OTOC [21–33] has become widely recognised and adopted in the high energy and condensed matter physics, despite initially being considered in the context of superconductivity [34].

The OTOCs, within the framework of quantum mechanics, are the growth of non-commutating quantum mechanical operators describing the *Unequal Time Commutation Relations* (UTCRs). It is the most potent quantum mechanical analogue of the classical sensitiveness to the initial conditions, despite of the fact that OTOCs measure this sensitivity in a scrambled time order (also known as Ehrenfest time) [35]. During this time, OTOC shows exponential growth. Unlike classical systems, quantum measurements inherently disturb the measured system, and the OTOCs measure this disturbance by considering both forward and backward time evolution as quantum corrections allow it to contain higher-order derivatives of $x(t)$.

Despite its utility, the relationship between OTOC and chaos is subtle. Several researchers have explored the behaviour of OTOCs in the context of chaos and potential functions. For instance, K. Hashimoto et al. [36], R. A. Kidd et al. [37], and B. Bhattacharjee et al. [38] have argued that exponential growth in OTOCs near a local maximum of a potential function may not necessarily indicate chaos. Supporting this view, Kirkby et al. [39] also claimed that relying solely on OTOCs to detect chaos can yield false signals. Xu et al. [40] further argued that exponential growth of OTOCs, often referred to as scrambling, does not inevitably imply chaos. Takeshi Morita [41] demonstrated that OTOCs for a localised wave packet representing a classical particle near a hill in the potential function exhibit exponential growth.

The primary focus of the aforementioned works is to observe the behaviour of OTOC near a saddle point of an integrable system. Naturally, the suitable candidates for such a study are a double-well potential, having an *inverted harmonic potential* (IHO) term. These stud-

---

[a] e-mail: pranayapratik_das@nitrkl.ac.in

[b] e-mail: biplabg@nitrkl.ac.in (corresponding author)

ies conclude that the exponential growth of the OTOC is a universal characteristic irrespective of integrability of the system, provided the potential includes a local maximum, indicating instability. This line of argument does not explore the deeper understanding of the general cause of exponential growth in OTOC. This raises an intriguing question: What happens if perturbed well does not have a local maximum? If the local maximum is the sole driver of exponential growth, then its absence should show no such behaviour in the OTOC.

To explore this, we consider one-dimensional quantum mechanical models with three specific polynomial potentials [36,41,42,44–46] with a linear perturbation term. We study the behaviour of OTOC and other chaos diagnostic tools while perturbation strength is varied. We extend the study when the saddle point disappears at a suitable perturbation. Such a perturbation introduces symmetry breaking in the system [47–55]. Understanding the interplay of bifurcation and symmetry breaking is crucial in investigating phenomena like flames, chemical reactions, biological pattern formation, stability analysis, and the onset of chaos in different systems [56–60].

As the saddle point disappears, the potential function becomes more asymmetric, driven by an asymmetric term (perturbation). Symmetry–asymmetry in the potential are seen in the classical bifurcation diagram and the structure of quantum eigenstates and eigenvalues [48]. Our primary objective is to quantify how asymmetry affects OTOCs: whether it amplifies, suppresses, or alters the pattern of exponential growth. To reinforce our findings, we employ additional chaos diagnostic tools, specifically the Loschmidt Echo, for all models in identical scenarios. This helps validate and complement our observations influenced by symmetry-breaking perturbations in quantum systems.

The structure of this paper is as follows. In Sect. (2), we discuss the formalism for computing the OTOC of a quantum mechanical system with a time-independent Hamiltonian. In Sect. 3, we devise three models, namely a double well, a double well with a plateau (Sect. 3.1), and a triple well (Sect. 3.2). In the individual subsections of the models, we perform a quantitative analysis to investigate the connection between the classical bifurcation diagram and symmetry breaking in the potential landscape, while varying different parameters. The introduction of perturbation disrupts the inherent symmetry within these potentials, leading to the emergence of asymmetric structures. Following the solution of the Schrödinger equations for these quantum mechanical models under specific perturbation strengths, we proceed to measure the microcanonical & thermal OTOCs and density of states. Section 3.3 contains our numerical observations on the above-mentioned three models using other chaos diagnostic tool, Loschmidt Echo. Subsequently, we summarise our results in Sect. 4.

2 OTOC in quantum mechanics for a time-independent Hamiltonian

A 2N-point thermal OTOC [22,27] is defined as:

$$C_\beta(t_1,t_2) = -\left\langle [\hat{x}(t_1),\hat{p}(t_2)]^N \right\rangle_T \tag{1}$$

where $\langle\rangle_T$ is the thermal average, $\beta = \frac{1}{k_B T}$, with k_B being the Boltzmann's constant, also known as "the coldness function". Additionally, $\hat{x}$ and $\hat{p}$ are, respectively, quantum mechanical operators for position and momentum.

While the $N=1$ case exhibits random but decaying behaviour, studying the $N=2$ case, involving the four-point correlator, provides a complete understanding of time disorder averaging. Exploring higher-order cases would be unnecessary for our study.

For simplicity, we take $t_1 = t$ and $t_2 = 0$ in Eq. (1), and define the four-point OTOC [61] as:

$$\mathcal{C}_\beta(t) = -\left\langle [\hat{x}(t),\hat{p}]^2 \right\rangle_T \tag{2}$$

Using the classical–quantum correspondence [62,63], $\frac{[,]}{i\hbar} \to \{,\}_{poisson}$, one can show its subtle relation with the classical Lyapunov exponent (λ_L) as follows:

$$\begin{aligned} \tfrac{1}{i\hbar}\langle[x(t),p(0)]\rangle \quad &\to \{x(t),p(0)\} = \tfrac{\partial x(t)}{\partial x(0)} \sim e^{\lambda_L t} \\ -\tfrac{1}{\hbar^2}\langle[x(t),p(0)]^2\rangle &\to \{x(t),p(0)\}^2 = \left(\tfrac{\partial x(t)}{\partial x(0)}\right)^2 \sim e^{2\lambda_L t} \end{aligned} \tag{3}$$

Thus, from the above semiclassical connection, OTOC quantifies the sensitivity of time evolutions in both chaotic and non-chaotic quantum systems to their initial conditions. In non-chaotic systems, fluctuations exhibit periodic, aperiodic, or irregular behaviour, whereas chaos is characterised by an exponential growth in the early stage followed by saturation in the later times [64–68]. Here, we assume that the classical–quantum correspondence can break down after the scrambling/Ehrenfest time, making it more challenging to detect exponential developments in quantum systems compared to classical ones [69]. The OTOC grows exponentially from time $t_D \sim \frac{1}{\lambda_L}$ to scrambling/Ehrenfest time $t_E \sim \frac{1}{\lambda_L}\log(\frac{1}{\hbar_{eff}})$ [29,35]. After that, it saturates depending on the size of the system. Note that the relation between the exponential growth rate of OTOC and the classical Lyapunov exponent is only valid for systems with a suitable semiclassical limit.

For a Hamiltonian with the form,

$$\mathcal{H} = \sum_{i=1}^{N} \frac{p_i^2}{2} + \mathcal{U}(x_1, x_2, ..., x_N), \tag{4}$$

and partition function,

$$Z(\beta) = \sum e^{-\beta\mathcal{H}} = \sum_{m} e^{-\beta E_m} \tag{5}$$

Equation (2) takes the form [36,42,64,70,71],

$$\mathcal{C}_\beta(t) = \frac{1}{Z(\beta)} \sum_m e^{-\beta E_m} c_m(t) \tag{6}$$

where $\mathcal{H}|m\rangle = E_m|m\rangle$ and

$$\begin{aligned} c_m(t) = \frac{1}{4} \sum_{k,l,r}^{n_{trunc}} x_{ml}\, x_{lk}\, x_{rm}\, x_{kr} \Big(& E_{rk}\, E_{lk} e^{itE_{rl}} \\ & + E_{mr}\, E_{ml} e^{-itE_{rl}} - E_{rk}\, E_{ml} e^{it(E_{rm}+E_{lk})} \\ & - E_{mr}\, E_{lk} e^{-it(E_{rm}+E_{lk})} \Big) \end{aligned} \tag{7}$$

where $n_{trunc} \in \mathbb{N}$, is the finite terms in the summation, used for calculation. Beyond this, the contribution in the summation is negligibly small due to exponential decay with higher energy.

We refer $c_m(t)$, in Eq. (7), for a fixed energy eigenstate as *microcanonical OTOC*[1] and $\mathcal{C}_\beta(t)$, in Eq. (6), as a *thermal OTOC.*[2] Here, $E_{nm} = E_n - E_m$, $x_{nm} = \langle n|\hat{x}|m\rangle$ and $p_{nm} = \langle n|\hat{p}|m\rangle$. Here, $p_{mn} = \frac{i}{2} E_{mn} x_{mn}$ Ref. (Appendix A, Eq. (A2)).

The OTOC is a direct measure of dynamical non-commutativity. If $\hat{x}(t)$ and $\hat{p}$ commute ($[\hat{x}(t), \hat{p}] = 0$), the OTOC vanishes. Therefore, nonzero OTOC directly reflects their non-commutativity. In chaotic systems, the OTOC grows exponentially ($\sim e^{\lambda t}$). The behaviour of the OTOC in quantum systems typically unfolds in three distinct temporal regimes [29,33,42,65,72]: early-time regime ($t < t_D$), intermediate-time regime ($t_D < t < t_E$), and late-time regime ($t > t_E$). These time regimes are closely tied to the system's dynamics, such as integrability, chaos, and thermalisation.

3 Models

The idea behind the choice of our models rests on the fact that a small symmetry-breaking perturbation term in a Hamiltonian disrupts the underlying symmetries of certain classical systems. This disruption triggers a cascade of nonlinear resonances within the broken symmetry regions. The emergence of these resonances often leads to the onset of chaos. As these regions grow, the chaotic nature of the system intensifies, resulting in increased unpredictability and complexity [48,73].

Let us consider, a Hamiltonian of the form of:

$$\mathcal{H} = \frac{-1}{2}\nabla_x^2 + V(x) + \ \Lambda *\ x \tag{8}$$

where

$$V(x) \rightarrow \text{Potential} \tag{9a}$$
$$\Lambda *\ x \rightarrow \text{Perturbation} \tag{9b}$$

We work in the natural units ($\hbar = k_B = 1$) and, without any loss of generality, we assume that the mass of the oscillator $m = 1$.

Double-well potential models that we have considered have an *Inverted Harmonic Oscillator* (IHO) [44,74–81] term. The IHO, a physically realised system, exhibits an unstable point at ($x = 0,\ p = 0$) in phase space. When perturbed, the particle undergoes exponential acceleration away from this fixed point, resulting in divergent solutions in phase space. $Model\ (I)$ (3.1), and $Model\ (I-a)$ (3.1.2: A special case), each has a distinct form of lower bounds and hilltops. Furthermore, $Model\ (II)$ (3.2) employs the Harmonic Oscillator (HO) potential form to create a triple-well configuration.

3.1 $Model\ (I)$: Double Well

For $Model\ (I)$, $V(x)$ is in the form of a nonlinear potential function:

$$V(x) = a_0\ \hat{x}^4 - a_1\ \hat{x}^2 \tag{10a}$$
$$\Lambda \ = \left(\sigma\sqrt{\left|\frac{a_0}{2\ a_1}\right|}\right), \tag{10b}$$

where a_0, a_1, and σ are known as stabilisation, destabilisation[3], and asymmetry parameter, respectively. Note that the term x^4 provides a lower bound to the potential[4], and the lowest bound is taken to be zero for all the models. The parameter Λ stands for the perturbation strength.

It is evident in this constructed system that the non-degenerate energy doublets have a splitting $\Delta = \sigma$, i.e. splitting between levels remains close to σ for all doublets lying below the barrier top. The initial inspiration for devising the model is taken from [82–85].

3.1.1 Bifurcations and symmetry breaking

The pitchfork bifurcation is commonly encountered in systems in which there is an overall parity symmetry

---

[1] OTOCs within the microcanonical ensemble, where the energy of the system is fixed, offer valuable insights into how information gets scrambled in quantum systems.

[2] The thermal ensemble, also known as the canonical ensemble, describes a system at a specific temperature. In contrast with the microcanonical ensemble, in the canonical or thermal OTOC calculation the temperature is fixed.

[3] a_0 determines the width of the wells and a_1 determines the curvature of the unstable top of the hill.

[4] Without the x^4 term in the potential, the system would not have any ground state and defining temperature (T) would have been impossible.

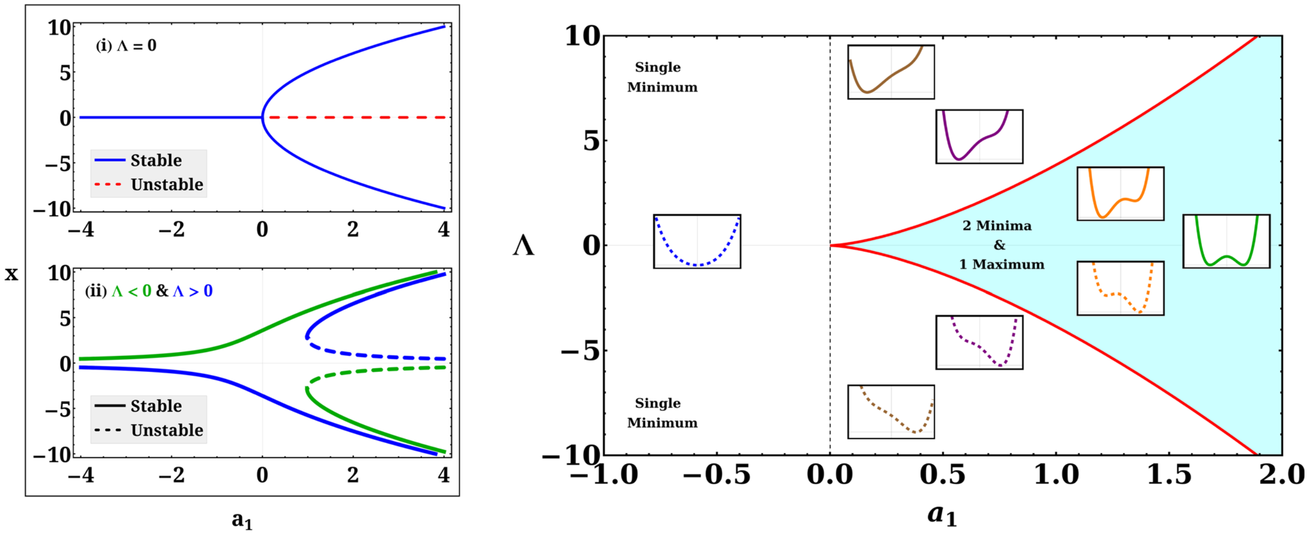

(a)

(b)

Fig. 1 Bifurcation and stability analysis graphs for *Model* (I). (**a**) A saddle-node bifurcation occurs at $a_1 = \dfrac{3}{2}a_0^{1/3}\Lambda^{2/3}$. $(a(i))$ For $\Lambda = 0$ this reduces to the supercritical pitchfork; $(a(ii))$ for finite Λ the pitchfork is deformed and even changed topologically. (**b**) Existence and stability domains of fixed points (or phase diagram) for the imperfect bifurcation in the $(a_1,\ \Lambda)$ plane are discussed. Here, the shaded region shows the domain where the system has three fixed points, and the plain white region shows the domain with one fixed point

$(x \to -x)$ [52,86–88], which has fixed points at $x^* = 0$ and $x^* = \pm\sqrt{\left|\frac{a_1}{2a_0}\right|}$. The imperfect bifurcation occurs when a symmetry-breaking term is added to the pitchfork. Here, the constant Λ breaks the parity symmetry. The bifurcation diagrams are shown in Fig. 1a, where Fig. 1a$-i$ shows pitchfork bifurcation when $\Lambda = 0$ and Fig. 1a$-ii$ shows the imperfect bifurcation when the $\Lambda \neq 0$. The system's solution space becomes asymmetrical because of the presence of finite Λ. The solutions now favour one direction over the other instead of being perfectly symmetric about the origin. This can lead to the emergence of new stable or unstable equilibrium points, depending on the specific magnitude of Λ. Consideration of stability analysis or fixed-point analysis around bifurcation points is necessary in order to determine how Λ affects the stability landscape.

The fixed-point analysis in Fig. 1b shows that the system can exhibit one or three fixed points (one global minimum, or a local maximum and two global minima). We shall restrict ourselves to the cases where the system has three fixed points. Hence, as long as $a_1 > 0$, the system has a double-well potential. Even though $\Lambda < 0$ gives the exact parity inverse of the potential as for $\Lambda > 0$, we shall restrict ourselves to the latter case where $\Lambda > 0$ for all our studies. Notice that this asymmetric double-well potential becomes symmetric when the relation $\Lambda = 0$ is satisfied.

The emergence of a maximum in a single well can also result from a symmetry-breaking perturbation (pitchfork bifurcation), provoking the system to transition into a lower symmetric state. Due to this symmetry breaking, the linear behaviour in $V'(x)$ becomes nonlinear and its value becomes zero at the bifurcation point. The nonlinear behaviour of $V'(x)$ quantifies the asymmetry in the potential. If we examine *Model* (I), as shown in Fig.2, we discover that $V'(x)$ has a singular positive minimum at $x = 0$, for $\sigma = 0$ (in fact here $V'(x) = 0$) , while progressively shifting towards positive x as σ increases. This implies the asymmetry in the potential spreads towards positive x. For a much higher value of σ, the minimum in $V'(x)$ is indistinguishable, implying no further spreading of asymmetry or deformation in the potential.

We solve the time-independent Schrödinger equation numerically, considering the Hamiltonian in Eq. (8) for the potential given in Eq. (10a) in `Mathematica 12.0` using `NDEigensystem` built-in command and obtain the energy eigenvalues E_n and the wave functions $\Psi_n(x)$. The results for *Model* (I) with $\sigma = 0$ are shown in Fig. 2a. Here, the eigenstates below the hilltop are almost degenerate even though the Hamiltonian and the potential are symmetric under space inversion [89–91]. Figure 2b, c and d shows the energy eigenvalues for σ having values 10.0, 30.0, and 70.0, respectively.

For numerical calculation, we consider the form of model potentials within a finite suitable range in x beyond which the potentials are taken as rigid wall. Such consideration does not affect our result. The suitable value of the range or width (L) is chosen by calculating eigenvalues as a function of L. For *Model* (I) and *Model* $(I - a)$, L is chosen as 20 (Ref. Appendix B).

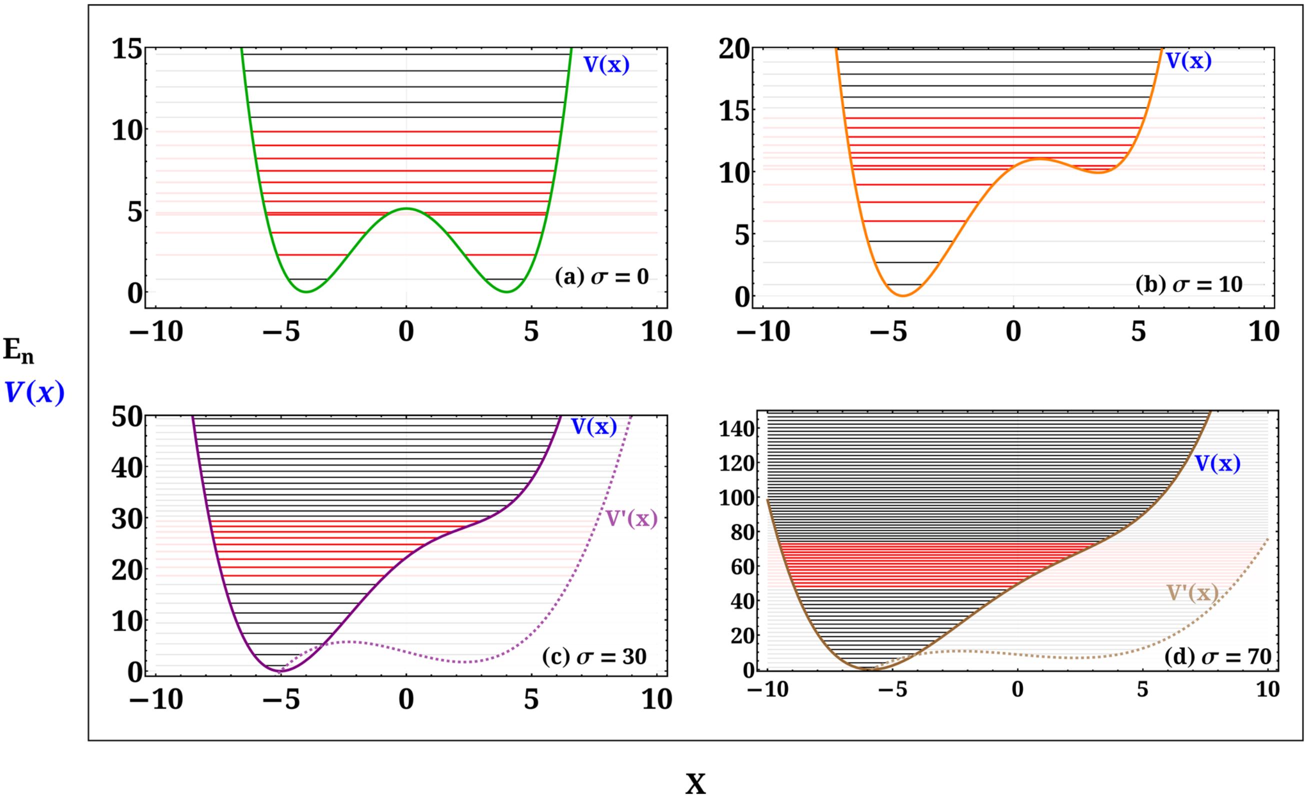

Fig. 2 Potential energy curves and energy eigenvalues for *Model* (*I*) with $a_0 = 0.02$, $a_1 = 0.64$ and **a** $\sigma = 0.0$ (two symmetric global minima), **b** $\sigma = 10.0$ (one global and one local minima), **c** $\sigma = 30.0$ (one global minima), (*d*) $\sigma = 70.0$ (one global minima). The energy levels below the top of the hill are almost degenerate, and the energy levels of the potentials in red colour show exponential growth in OTOC. Whenever the slope of the potential ($V'(x)$) at the classical turning point is a positive minimum, the energy density is maximum around that turning point

3.1.2 OTOC analysis

In Fig. 3, the microcanonical and thermal OTOCs are presented in four consecutive rows, with $\sigma = 0,\ 10,\ 30$ and 70. The left column shows the graphs of the microcanonical OTOCs, while the right column displays the corresponding thermal OTOCs. Each row of graphs represents a specific value of σ. The microcanonical OTOC for $\sigma = 0$ display exponential growth within a small energy eigenfunction range (from $n = 4$ to 15) around the local maximum of the potential at $E = 5.12$, as shown in Fig. 3a. Furthermore, we compute the thermal OTOCs for various values of the temperature as shown in Fig. 3b. The numerical findings show exponential growths as temperatures rise. Figure 3b, d, f, and h (black dotted line) shows that exponential growth in thermal OTOC occurs for those eigenstates for which the microcanonical OTOC shows exponential growth. There is a strong correlation between them.

We also observe the exponential growth of OTOCs for $\sigma = 10.0$ around the summit of the potential function. It should be noted that as the asymmetry parameter increases, the hilltop in the potential function vanishes. This causes an increase in the number of states exhibiting exponential growth. These two outcomes ($\sigma = 0$ & 10) agree with the findings of [36,40]. The local maximum disappears for $\sigma > 15.7656$ or $\Lambda > 1.9707$ $(= \frac{2}{3}\sqrt{\frac{2a_1^3}{3a_0}})$. In the present case ($\sigma = 30.0$), both microcanonical and thermal OTOCs display sustained exponential growth (Fig. 3e and f) within the Ehrenfest time scale in the absence of local maximum. Here, the number of energy levels that show exponential growth ranges from $n = 10$ to 18. At $\sigma = 70.0$ (Fig. 2d), the deformation on the potential curve further smoothens. Here, energy levels from $n = 21$ to 35 exhibit exponential growth in microcanonical OTOC (Fig. 3g), albeit with the shortest growth duration. However, in this case, the thermal OTOC shows no such growth, Fig. 3h.

In the thermal analysis plots, the average microcanonical OTOC, $= \langle \log_e[c_n(t)] \rangle$, closely tracks the thermal OTOC behaviour in the intermediate temperature range for $\sigma = 0$ & 10. However, for $\sigma = 30$ & 70, we find imperfect fits. This is because we have ignored a significant number of states exhibiting short-time exponential growth, considering our primary focus on the long-time exponential behaviour. As a result, the number of excluded states is comparable to the number of states included in the average. This suppresses the actual behaviour of $= \langle \log_e[c_n(t)] \rangle$, and consequently,

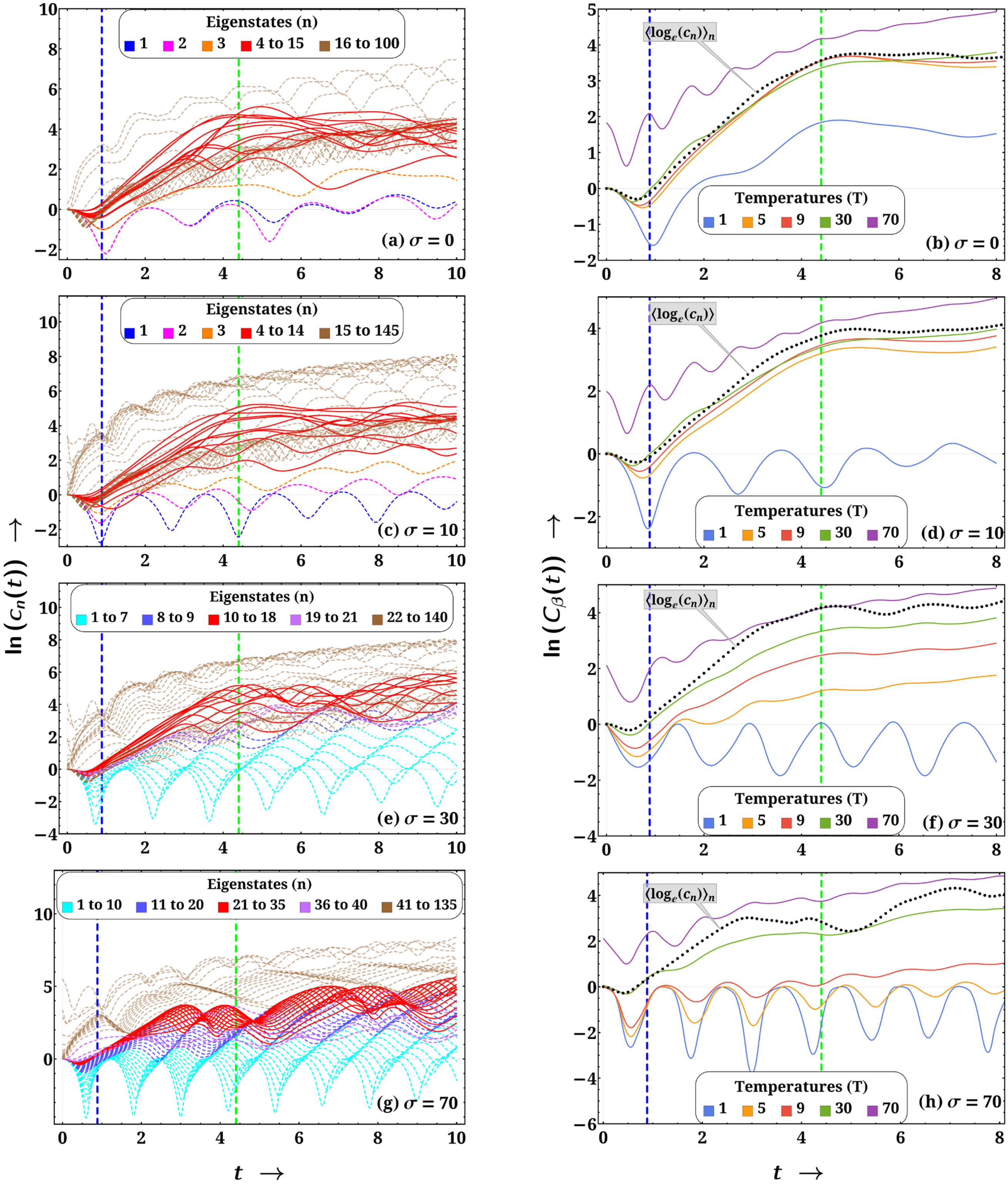

Fig. 3 Microcanonical and thermal OTOCs for *Model* (*I*) for different values of σ are in the left and right columns, respectively. The exponential growth that occurred in the early times between $t_D \sim 0.88$ (blue dashed line) and $t_E \sim 4.42$ (green dashed line) is illustrated in "red" colour for microcanonical OTOC. The average microcanonical OTOC for these states is represented by the black dotted line in the thermal OTOC plots (right column)

the dashed line appears to stretch beyond the genuine thermal ensemble behaviour.

In each of these cases, the OTOCs for higher energy eigenstates initially show brief periods of growth followed by irregular oscillations or fluctuations. The brevity of this growth phase makes it challenging to discern its precise nature, whether it follows a linear, exponential, or polynomial pattern. Nevertheless, this pattern suggests that the influence causing exponential growth in the lower energy eigenstates diminishes as we move to higher energy levels. The irregular fluctuations indicate a transition to a more regular behaviour.

Figure 4a illustrates the difference between successive energy eigenvalues. The presence of distinct dips in all curves (highlighted in red) signifies regions of higher density of states in specific energy ranges. The initial oscillatory pattern (black dashed lines) observed for $\sigma = 0$ and $\sigma = 10$ arises from the near-degeneracy of eigenstates below the hilltop. As the asymmetry increases with the increase of σ values, degeneracy is lifted from the system, resulting in a smooth dip in the difference curve for $\sigma =$ 30 & 70. Additionally, the figure includes insets displaying the density of states for the corresponding σ values, providing an alternative perspective on the same phenomenon. Notably, the eigenstates belonging to these regions (red highlighted regions) show exponential growths in OTOCs.

The graphs provide compelling evidence that the eigenstates, which show an exponential growth in the OTOCs, are tightly clustered together. This dip is near to the energy, where the slope of the potential($V'(x)$) is minimum at the classical turning point, having positive value. The nonlinear change of slope indicates deformation or asymmetry in the potential. In the case of a symmetric double well, this cluster happens to be located in close proximity to the hilltop.

Figure 4b then highlights several selected eigenstates that show this exponential growth. The evidence suggests that, unlike the eigenstates that do not show an exponential growth of OTOCs, these particular states are highly localised.

OTOC plots in Fig. 3, energy-level density in Fig. 4a, and the probability distribution of eigenstates in Fig. 4b for $Model\ (I)$ show a strong co-relation among all these quantities and with the asymmetry in the potential. These figures show that exponential growth in OTOCs emerges for those energy levels which are closely packed. These energy levels are in the neighbourhood of the classical turning point of the potential where the slope ($V'(x)$) is a positive minimum. The energy difference curve (Fig. 4a) dips to a minimum value where the slope of the potential has a positive minimum. The corresponding eigenfunctions, near the turning points, oscillate comparatively with higher amplitude, resembling Airy function [92,93]. As a result, these energy eigenstates and their probability distribution have maximum spread over this region. The clusters of eigenstates involved in this behaviour lag behind or reach up to the dip on the energy difference curve.

A special case: Double-well potential with a plateau ($Model\ (I-a)$)

As a special case, we consider a double-well potential with a plateau [41,43] whose lowest power is quartic rather than quadratic. Unlike hilltop which implies an unstable point in phase space, plateau implies a neutral equilibrium position (i.e. $\frac{\partial^2 V(x)}{\partial x^2}\big|_{x=0} = 0$). This double-well potential is defined as below:

$$V(x) = a_0\ \hat{x}^6 - a_1\ \hat{x}^4 \tag{11}$$

where $a_0 = \frac{1}{142}$, $a_1 = 0.15$, x^4 produces a plateau instead of a hilltop and x^6 term gives a lower bound to the potential. As compared to $Model\ (I)$, this modified model ($Model\ (I-a)$) has a flat top (plateau), i.e. a neutral equilibrium position.

Similar to $Model\ (I)$, here also Λ breaks the parity symmetry leasing from pitch fork bifurcation to imperfect bifurcation. In Fig. 5a, the potential structure and corresponding energy eigenvalues for $\sigma = 0.0$ and 50.0 are shown. Notably, with the increase in asymmetry strength, the plateau disappears entirely for $\sigma > 38.9561$ or $\Lambda > 5.96857$ $(= \frac{16}{25}\sqrt{\frac{2a_1^5}{5a_0^3}})$.

Contrary to previous studies (i.e. unstable equilibrium is the main factor driving the exponential growth of OTOCs), we observe that the microcanonical OTOC shows exponential growth for energy levels near the plateau (from $n = 3$ to 15) for $\sigma = 0.0$ (Fig. 6a). The effect of plateau is to bring the OTOC of these states close to each other, forming a band and having almost the same growth rate. Accordingly, the exponential behaviour of thermal OTOC is also shown in Fig. 6b for higher value of temperatures. Similar behaviour persists for $\sigma > 0$ (when asymmetry increases) including, $\sigma = 50$, when the plateau is absent. As in the previous model, exponential growth of OTOCs exists for a slightly shorter period than the Ehrenfest time for $\sigma \gg 38.9561$. And, for intermediate temperatures, the behaviour of $\langle \log[c_n(t)] \rangle$ closely approximates that of the thermal OTOC. Here also we can find a corelation among OTOCs, energy eigenvalue distribution, the structure of eigenstates, and symmetry in the potential landscape (Fig. 5b).

The presence of plateau provides positive minima in $V'(x)$ over a range of x. This causes the exponential growth of OTOCs for closely packed energy levels to have the same growth rate (Fig. 6). The symmetry-breaking bifurcation in the quartic case is topologically equivalent to the quadratic case. Therefore, the energy difference curve (Fig. 5b) and eigenstate dynamics are similar across both the models, albeit with different curvature scales.

3.2 $Model\ (II)$: Triple Well

Triple-well potentials can be used as a building block for quantum gates and algorithms because of their unique tunnelling dynamics and ability to support multiple

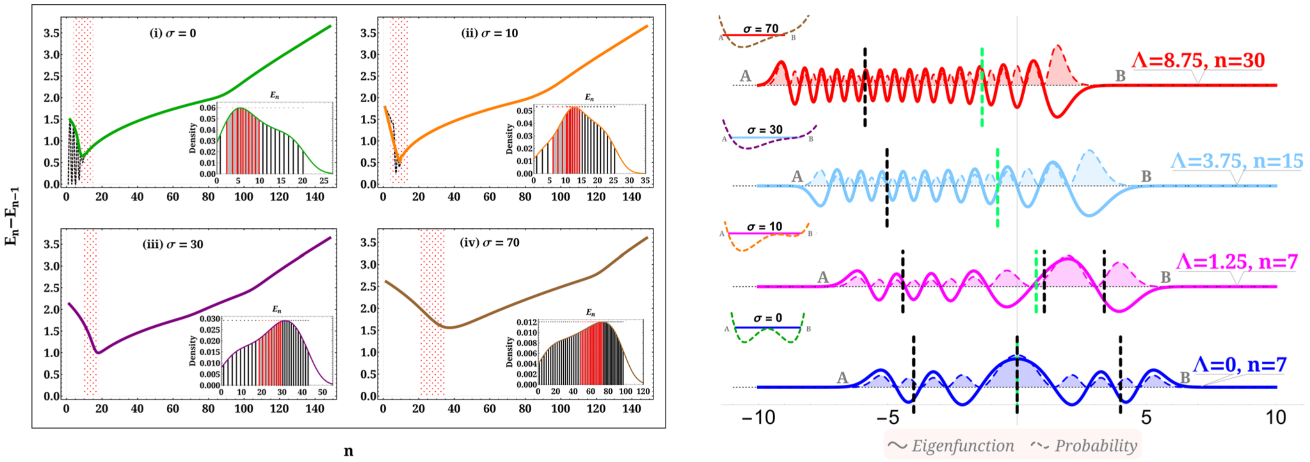

(a) (b)

Fig. 4 **a** Difference in successive energy eigenvalues as a function of quantum number n for different values of σ. Inset plots show density of states. **b** shows that probability amplitude increases towards right for all values of σ except for $\sigma = 0$ for sates that show exponential growth in OTOCs. Notice that mismatch in the positions of $\langle x \rangle$ (vertical green dashed lines) and the positions of equilibria (vertical black dashed lines) indicates asymmetry in the potential

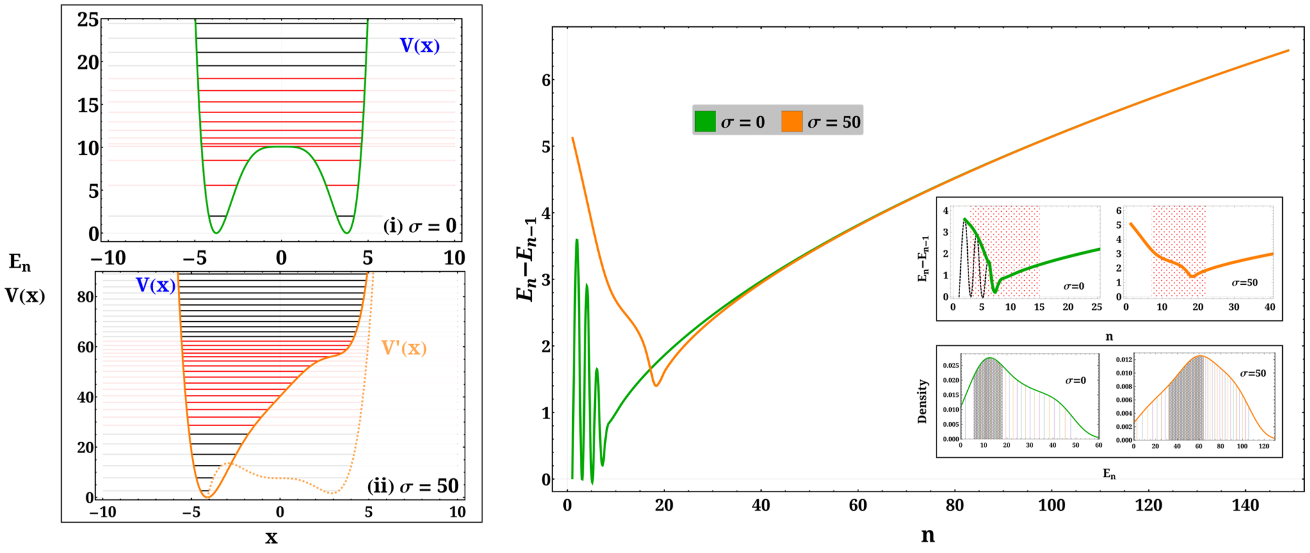

(a) (b)

Fig. 5 Potential energy curves and energy eigenvalues for $Model\ (I-a)$ with $(a(i))\ \sigma = 0.0$, $(a(ii))\ \sigma = 50.0$. The energy levels below the top of the hill are almost degenerated, and the energy levels in red colour show exponential growth in the OTOC. (b) Difference in successive energy eigenvalues as a function of eigenstates for different values of σ. Inset plots show density of states. On the difference curve, the decreasing slope region is shaded in red. Whenever the slope of the potential $(V'(x))$ at the classical turning point is a positive minimum, the energy density is maximum around that turning point

quantum states. Therefore, it plays a crucial role in various quantum computing and quantum information science applications [94–96]. Their applications extend beyond quantum computing to quantum simulations [97,98], metrology [97], error correction, and molecular dynamics, making them a key area of research in modern quantum technologies.

This model is primarily inspired by the work on [44–46,99,100]. The potential in Eq. (9a) for this case is

$$V(x) = a_1\ x^2 - a_0\ x^4 + x^6 \tag{12}$$

where $a_0 = 10.95445$, $a_1 = 30.0$. Here, $L = 10$.

3.2.1 Bifurcation and symmetry analysis

In Fig. (7a), for $\Lambda = 0$, the system always has a central minimum, along with two more minima of variable depths on either side of it depending on the value of a_0[5]. When Λ has a finite value, there is the potential loss parity symmetry, ending up in an asymmetrical

---

[5] For $9.5 < a_0$, we have a deformed single well potential. While for $9.5 < a_0 < 10.95445$, the central well is deeper, for $a_0 > 10.95445$, either side wells are deeper than the central well.

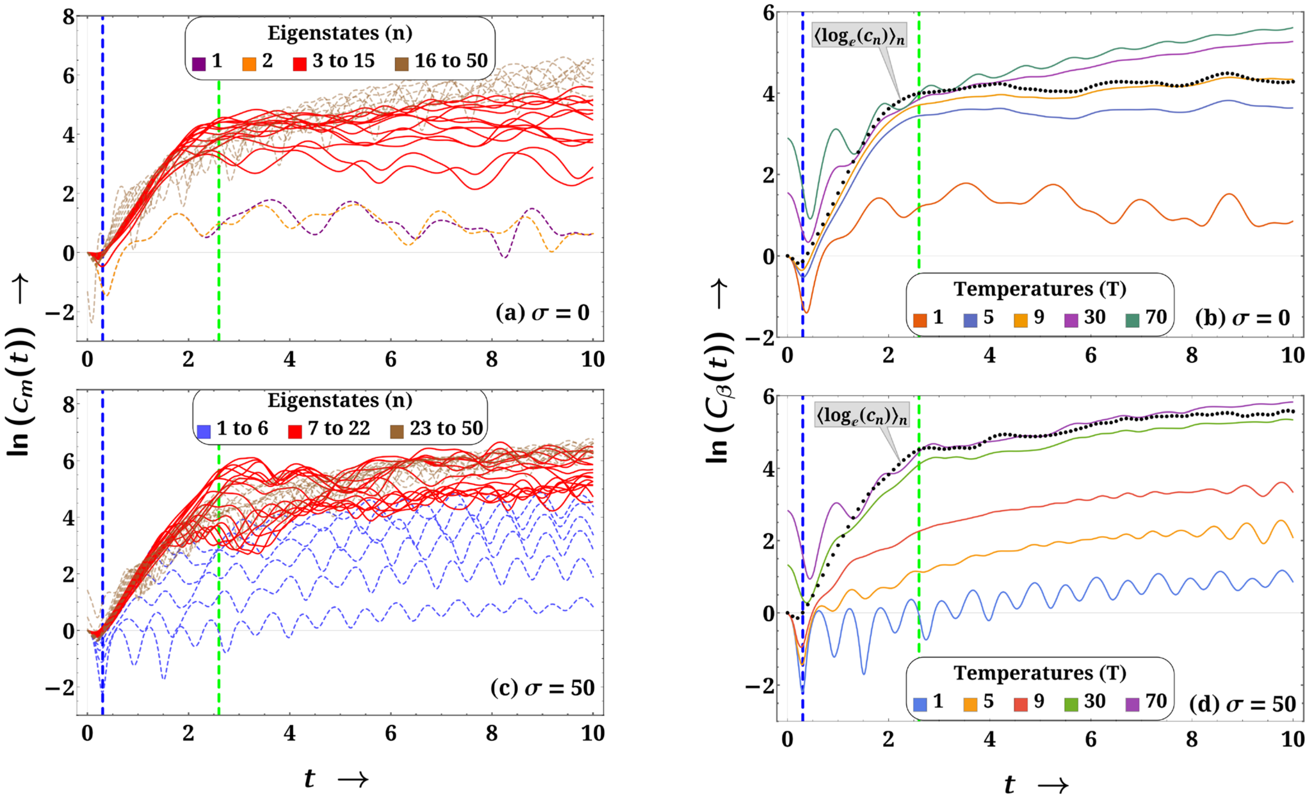

Fig. 6 **a**, **c** shows microcanonical OTOC and **b**, **d** shows thermal OTOC for $Model\ (I-a)$ with different values of σ. The exponential growth that occurred in the early times between $t_D \sim 0.3$ (blue dashed line) and $t_E \sim 2.6$ (green dashed line) is illustrated in "red" colour for microcanonical OTOC. The average microcanonical OTOC for these states is represented by the black dotted line in the thermal OTOC plots (on the right column)

solution space. The solutions now favour one direction over the other instead of being symmetric about the origin (central minimum). This leads to the emergence of new stable or unstable equilibrium points. In order to assess the impact of Λ on the stability landscape, stability analysis or fixed point analysis is performed around bifurcation points, as shown in Fig. (7b). Here, we have restricted ourselves to the cases where the system has five fixed points with $\Lambda \geq 0$, although $\Lambda < 0$ gives the exact parity inverse of the potential as for $\Lambda > 0$.

Figure (8) shows the eigenvalue solution to the Schrödinger equation for the $Model\ (II)$ potential with energy eigenvalue distributions under different values of σ. At $\sigma = 0$, the eigenstates below the hilltops are non-degenerate. $\sigma > 90$ ensures the absence of a local maximum in the potential function. However, the energy-level densities are found to be higher near two locations where the 1^{st} derivative of the potential ($V'(x)$) has two positive local minima. The exponential growth of OTOCs is restricted to the eigenstates found in these regions.

3.2.2 OTOC analysis

In Fig. 9a, the microcanonical OTOC exhibits exponential growth around the hilltops of the potential at $E = 24.3414$ for $\sigma = 0$. The energy eigenstates involved in this behaviour span from $n = 5$ to 16, with their energy ranging from 17 to 51. The exponential growth in thermal OTOC at higher temperatures is greatly influenced by these energy levels, as shown in Fig. 9b.

In Fig. 8b, at $\sigma = 95$, the microcanonical OTOC showcases exponential growth in two distinct energy-level clusters (higher energy-level densities) well separated along the potential landscape (Fig. 9c). The first cluster spans from $n = 3$ to 11 (black lines), while the second spans from $n = 18$ to 24 (solid red lines). An important point is that the microcanonical OTOC for the second cluster (solid red lines) exhibits a marginally prolonged exponential growth with respect to time as compared to the first cluster (black lines). While the mean saturation time for the first cluster falls behind t_E, for the second cluster, the mean duration is greater than t_E. However, as shown in Fig. 9d, the thermal OTOC exhibits exponential growth for higher temperatures for a time that is the mean of microcanonical OTOC durations of the two distinct energy-level clusters. In the temperature window between low and high extremes, $\langle \log[c_n(t)] \rangle$ follows the thermal OTOC pattern for both σ values.

The eigenstates, from $n = 12$ to 17, show a complex, non-monotonic pattern: initial short exponential growth, then partial saturation, then again slightly extended exponential growth before final saturation.

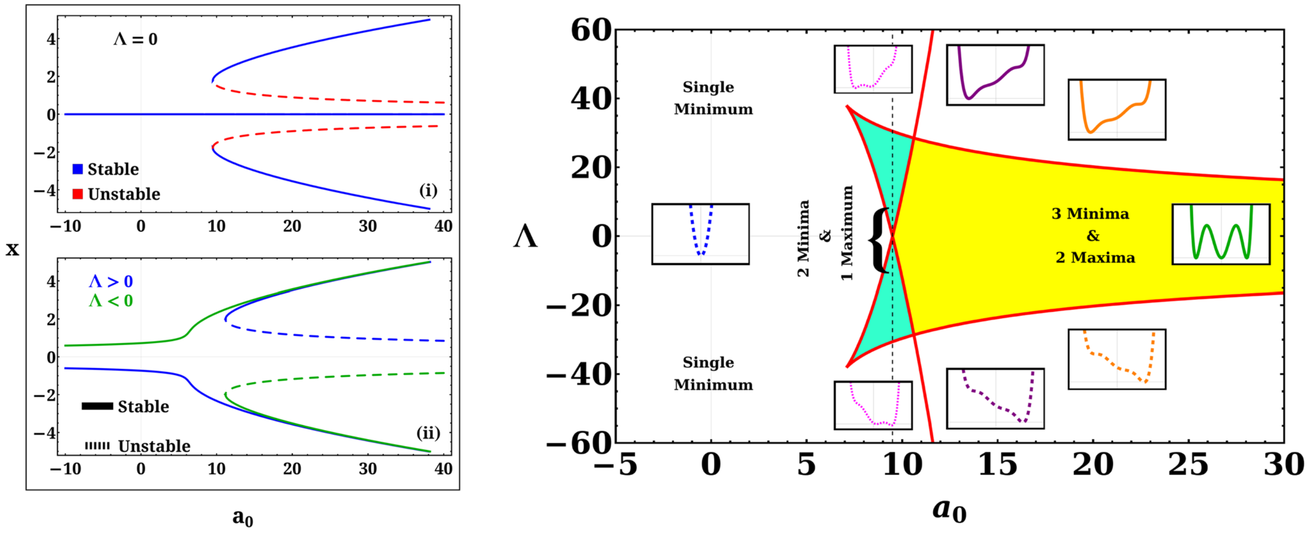

(a)

(b)

Fig. 7 Bifurcation and stability analysis graphs for *Model* (*II*). **a** Bifurcation Diagram. **b** Existence and stability domains of fixed points for the imperfect bifurcation in the (a_0, Λ) plane. Here, the yellow region shows the domain where the system has five fixed points, the cyan region contains the domain with two fixed points, and the plain white region shows the domain with one fixed point

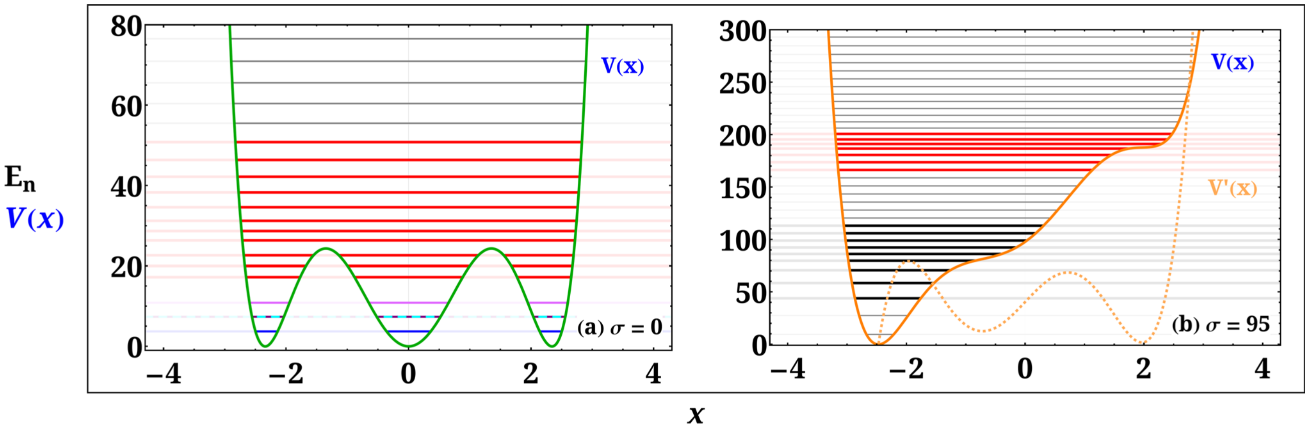

Fig. 8 Potential energy curves and energy eigenvalues for *Model* (*II*) with different values of σ. **a** For $\sigma = 0$ (three global minima & two local maxima), 2^{nd} energy level is nearly doubly degenerate represented in solid and dashed lines. **b** For $\sigma = 95$ (one global minimum). The energy levels in the red colour exhibit exponential growth in OTOC. Whenever the slope of the potential ($V'(x)$) at the classical turning point is a positive minimum, the energy density is maximum around that turning point

Since on the semi-logarithmic plot (Fig. 9c), microcanonical OTOC for these states does not show a strict linear behaviour, hence, we cannot count these as pure exponential growth. This behaviour is the remnant of the two nearby positive minima on $V'(x)$ curve, responsible for two high-level densities.

In Fig. 10a, we can see the successive differences in energy eigenvalues. The red shaded areas represent a higher density of states. For $\sigma = 0$, following an initial oscillatory trend, a prominent decline emerges in the curve, representing a higher density of states. At $\sigma = 95$, we can identify two distinct and well-separated dips in the curve. The first dip appears (in black shaded regions) to have a slightly shallower depth than the second (in red shaded regions), suggesting a higher density of energy eigenstates near the second dip. Observations suggest that there is a similar trend in the successive energy difference curve for higher values of σ. Figure 10a also incorporates insets of the density of states graphs for different σ values, offering an alternative viewpoint of the same analysis. The eigenstates belonging to these regions (red and black shaded regions) show exponential growths in OTOCs. These graphs offer clear evidence that the eigenstates, which show an exponential growth in the OTOCs, are tightly clustered together. This dip is near to the energy, where the slope of the potential is minimum at the turning point, having positive value.

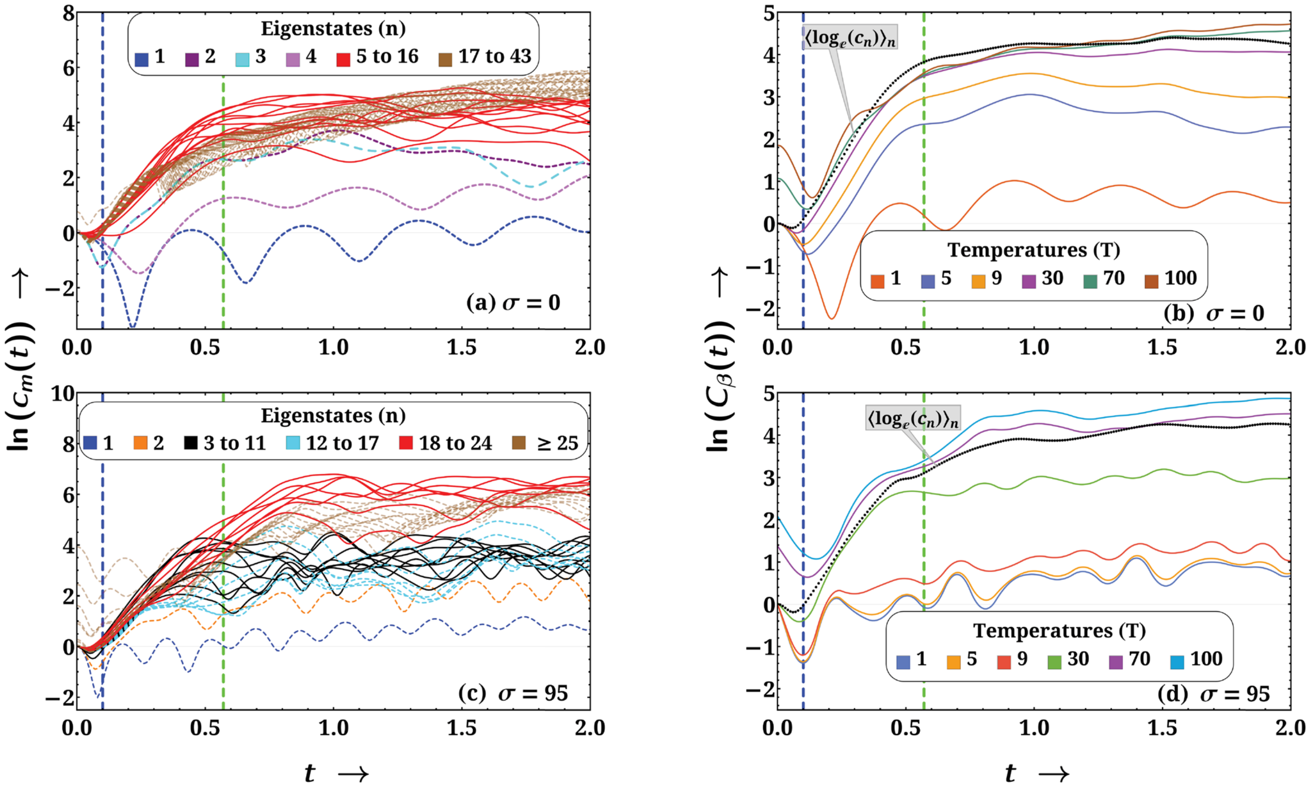

Fig. 9 Microcanonical and thermal OTOCs for *Model (II)* are shown in pairs in (**a**) & (**b**), and (**c**) & (**d**), respectively, with $\sigma = 0$ and 95. The exponential growth that occurred in the early times between $t_D \sim 0.1$ (blue dashed line) and $t_E \sim 0.57$ (green dashed line) is illustrated in "red" & "black" colour for microcanonical OTOC. The average microcanonical OTOC for these states is represented by the black dotted line in the thermal OTOC plots (right column)

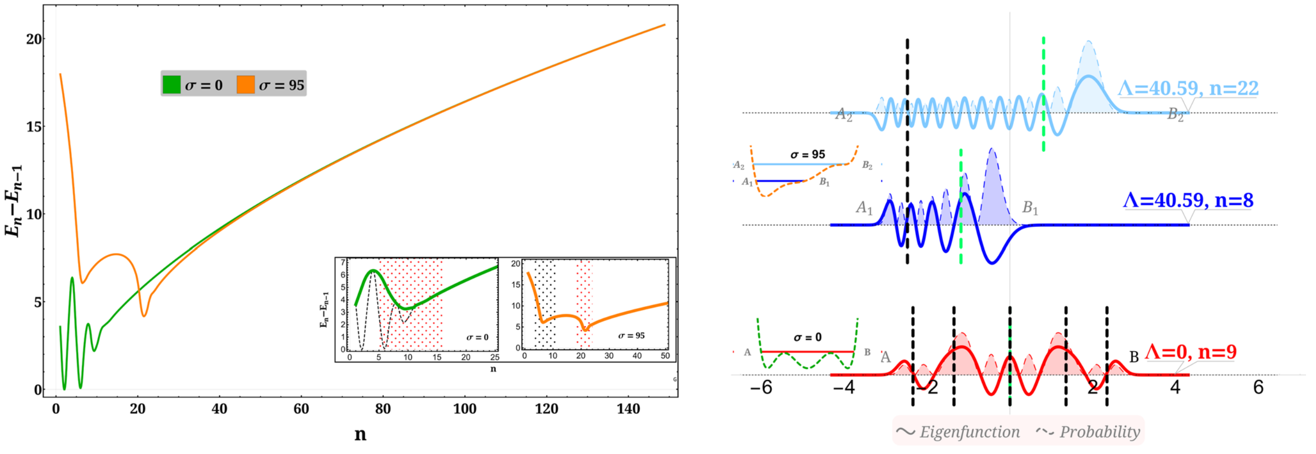

(a)

(b)

Fig. 10 **a** Difference in successive energy eigenvalues as a function of eigenstates for different values of σ. Inset plots show density of states. **b** shows that probability amplitude increases towards right for all values of σ except for $\sigma = 0$ for sates that show exponential growth in OTOCs. Notice that mismatch in the $\langle x \rangle$ (vertical green dashed lines) and the positions of equilibria (vertical black dashed lines) indicates asymmetry in the potential

Here, two maxima arise in a single well because of symmetry-breaking perturbation, after which the system ends up in a lower symmetric state. Perturbation gives rise to two simultaneous positive minima in $V'(x)$. As with $Model\ (I)$, these two minima in $V'(x)$ shift towards positive x as we increase the strength of linear perturbation. Due to asymmetry, one of the minima becomes local and the other global. The global minimum in $V'(x)$ is slightly sharper than the local. Our investigation of OTOC (Fig. 9), energy-level density (Fig. 10a), and probability distribution of eigenstates (Fig. 10b) correspond to these two minima points in $V'(x)$.

The dips in the energy difference curve (Fig. 10a) are at energies, which are, respectively, equal to the turning points on the potential function where two positive minima of the slope occur. The higher dip corresponds to the local minimum, whereas the lower dip corresponds to the global. The lower dip (high density) is due to sharper curvature at the global minimum. Similar to $Model\ (I)$, here also we observe the probability amplitude of eigenstates enhances towards right. The eigenstates belonging to the high density of states show longer time exponential growth as compared to the eigenstates belonging to low density of states.

The probability density of eigenstates (Figs. 4b & 10b) has a strong connection with the classical phase space structures. As illustrated in Fig. 11, the classical trajectories (coloured lines in the phase space diagrams) are less dense and elongated where the derivative of the potential, $V'(x)$, attains a local positive minimum. This structural feature of the classical dynamics manifests quantum mechanically as an increased probability amplitude of eigenstates skewed towards the right side of the potential landscape under the influence of perturbation. Interestingly, the OTOCs also exhibit exponential growth when $V'(x)$ is a positive minimum.

Summing up the result on the above models, we confirm a clear correlation among the OTOCs' exponential growth, the local density of energy levels, and the probability distribution of eigenstates (spatial spread), and symmetry breaking in the potential. First, we observe that exponential growth of OTOC, preferentially, occurs for clusters of closely spaced eigenstates that lie near the classical turning points, precisely where the potential slope, $V'(x)$, exhibits a shallow positive minimum. The energy difference curve shows a dip at these energy levels, indicating higher local density. In each of these cases, the clusters of eigenstates that show exponential growth in OTOCs lag or reach up to the dip on the energy difference curve. The corresponding eigenfunction concurrently displays amplified oscillations, analogous to an Airy function around the classical turning points, thus maximising probability density in these regions. In summary, the curvature of $V'(x)$ controls the density of states, eigenstate structure and the exponential behaviour of OTOC.

In a recent publication [101], the author has taken an inverted anharmonic (pure quartic) oscillator ($V(x) = -x^4$) and showed that OTOC shows oscillatory behaviour despite the classically unstable nature of the system. In the light of the above argument, we see that the potential $V(x) = -x^4$ does not have classical turning points and so it is not bounded from both sides. Therefore, there is no question of $V'(x)$ having a positive minimum at the turning point. That is why, it is not showing any exponential growth in OTOC. This result validates our findings.

3.3 Loschmidt Echo

Loschmidt Echo measures the revival occurring under an imperfect time-reversal procedure applied to a complex quantum system. This tool quantifies the sensitivity of quantum evolution to isospectral perturbations.[6] Any spectral quantity will remain unaffected, but the Loschmidt Echo will generally decay [102–109].

The Loschmidt Echo exhibits different decay behaviours depending on the strength and nature of the perturbation, complexity, dimension, and initial state of the underlying quantum system, discussed in references [20, 104, 110]. For global perturbation, there are different decay regimes. As perturbation strength increases from zero, the decay rate initially shows Gaussian [111–113] and then Fermi's Golden Rule [17, 111]. This growth finally gets saturated at the classical Lyapunov exponent from a critical value of perturbation strength and remains so within the range of interest of perturbation [17]. For local perturbation, the behaviour of decay rate is similar to the global except that instead of getting saturated, it oscillates around a much lower value of Lyapunov exponent [110].

Mathematically, the Loschmidt Echo is then defined as

$$M(t) = \left|A(t)\right|^2 = \left|\left\langle \Psi_0 \middle| e^{i\hat{\mathcal{H}}_2 t/\hbar} e^{-i\hat{\mathcal{H}}_1 t/\hbar} \middle| \Psi_0 \right\rangle\right|^2 \quad (13)$$

where $\mathcal{H}_2 = \mathcal{H}_1 + \Lambda x$ and $A(t)$ is the Loschmidt amplitude. A(t) quantifies the "distance" (in the Hilbert space) between the state $e^{-i\hat{\mathcal{H}}_1 t}|\Psi_0\rangle$, resulting from the initial state $|\Psi_0\rangle$ in the course of evolution through a time t under the Hamiltonian $\mathcal{H}_1$, and the state $e^{-i\hat{\mathcal{H}}_2 t}|\Psi_0\rangle$ obtained by evolving the same initial state through the same time t, but under a slightly different perturbed Hamiltonian $\mathcal{H}_2$. The LE, by construction, equals unity for t = 0 and typically decays further in time.

Perfect recovery of $|\Psi_0\rangle$ would be achieved by choosing $\Lambda = 0$, i.e. $\mathcal{H}_2 = \mathcal{H}_1$, which leads to $M(t) = 1$, but this is an impossible task in realistic problems and $M(t)$ is usually a decreasing function in t. The notion of time reversal, i.e. a backward time evolution from t to 0 under $\mathcal{H}_2$, is equivalent to the forward evolution between t and $2t$ under the Hamiltonian $-\mathcal{H}_2$.

For regular systems, $M(t)$ must oscillate with a fairly large amplitude. Strictly speaking, $M(t)$ is almost periodic. On the other hand, if $\mathcal{H}_1$ is chaotic, $M(t)$ is small.

---

[6] No change in the spectrum of the unperturbed Hamiltonian.

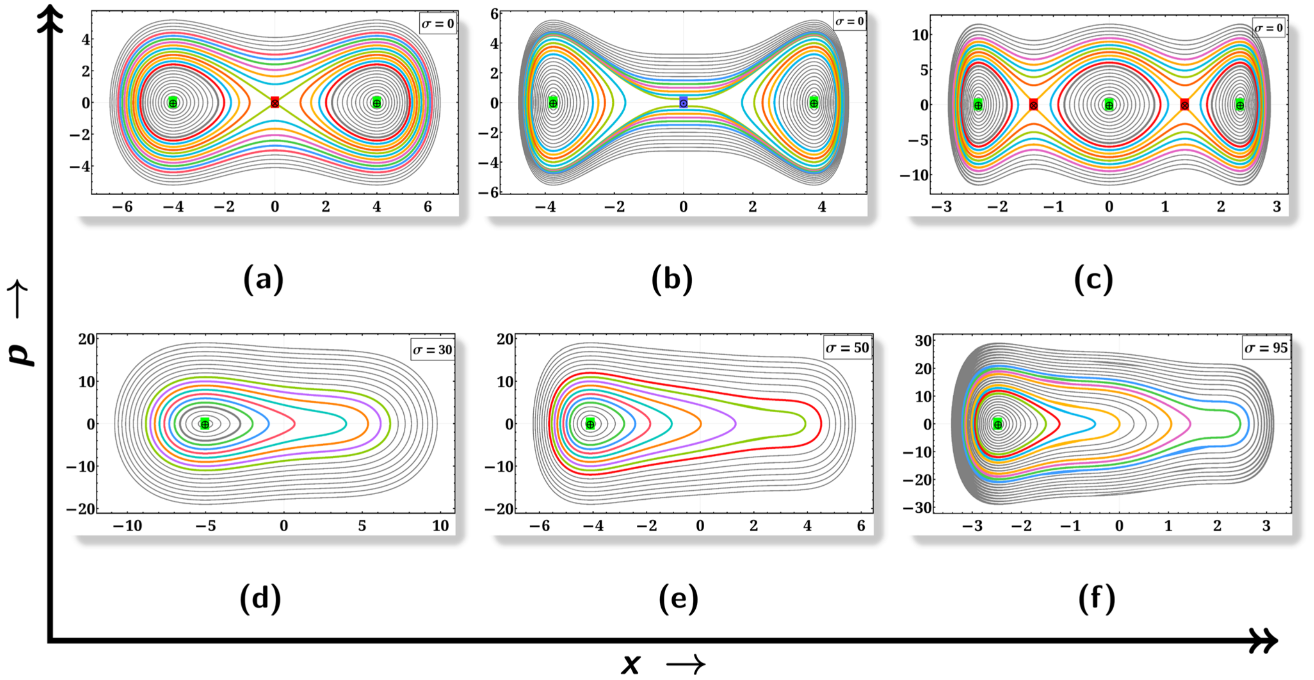

Fig. 11 Classical phase space diagram showing spatial stretching of trajectories at different energy. ⊕, ⊗, and ⊙ points are the stable, unstable and neutral equilibrium points, respectively. The top row corresponds to systems with symmetric potentials with no perturbation ($\sigma = 0$). Meanwhile, the bottom row represents the phase space structure of perturbed potentials

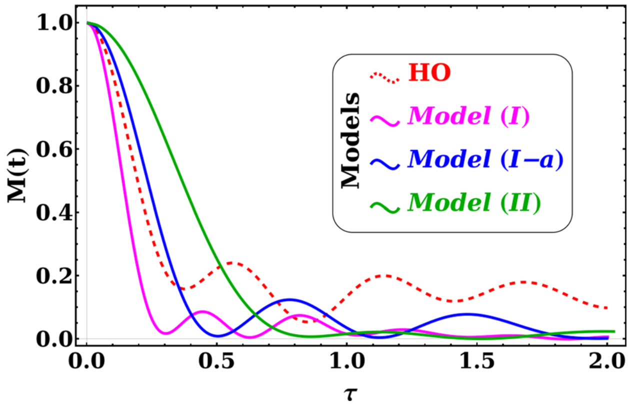

Fig. 12 Loschmidt Echo of HO *Model* (I), *Model* $(I-a)$, and *Model* (II). Here, $\tau = \dfrac{\Lambda t}{\hbar}$. Except for HO, other models show oscillation in Loschmidt Echo ($M(t)$) close to zero validating exponential growth in OTOCs

Another fact is that the initial decay rate of $M(t)$ for regular systems is fairly the same as for chaotic systems.

For varying Λ values, our numerical investigation reveals an initial exponential decay followed by anticipated low-amplitude oscillations in the LE. Figure 12 illustrates the compilation of LEs encompassing the *Harmonic Oscillator* (HO), as well as *Models* (I), (II), and $(I-a)$. In particular, after the initial decay, the LE displays significant amplitude fluctuations in the HO case. However, intriguingly, our investigated models demonstrate comparatively smaller fluctuations in their LE behaviour. This contrast in fluctuation amplitude between the HO and our models suggests the presence of distinctive dynamical behaviours, potentially indicating unconventional characteristics in our systems.

Prior works [72,107] have firmly established a relationship between OTOC and LE. Exponential growth in OTOCs corresponds to small oscillation in LE after the initial decay. Our calculations for perturbed systems without hilltops also show small amplitude oscillations in all the chosen models. This aligns with our observations of OTOCs.

4 Conclusion

Several earlier researches have shown that for the potentials having a hilltop, OTOCs show exponential growth for the eigenstates near the hilltop. The reason for such behaviour is attributed to the instability due to the hilltop. Our study on perturbed harmonic oscillators, having one and two hilltops and a plateau, demands that it requires a deeper understanding of such a behaviour. Our study sheds light on how asymmetry in the potential impacts the properties of energy difference, eigenstates, and OTOCs. This study can also explain the exponential growth of the OTOC, even in the absence of any hilltop.

To see the role of asymmetry in potential, we consider unperturbed potentials having a hilltop, a plateau and two hilltops. In all the cases, a linear perturbation breaks the symmetry of potential landscape and eventually, for a certain perturbation, no hilltops appear. In all the cases, our OTOC calculations show it grows exponentially for a range of eigenstates around the energy, which is equal to a classical turning point of the potential at which $V'(x)$ is a positive minimum. The difference in successive energy eigenvalues is minimum at this energy. The probability distributions of eigenstates are the maximum around the point where $V'(x)$ is a positive minimum. Our calculation of the Loschmidt Echo confirms the behaviour of OTOCs. These observations clearly indicate a strong correlation among exponential growth in OTOC, energy eigenvalue distribution, the structure of eigenstates, and asymmetry in the one-dimensional potential landscape. Since one-dimensional potentials do not show classical chaos, the corresponding quantum system cannot show chaos. Therefore, these tools alone cannot be confirmatory diagnostic tools of quantum chaos. However, our results suggest: by inspecting the minima on the slope of a quantum potential, one can predict where eigenstates will be most localised and can selectively control which spectral bands exhibit rapid OTOC growth. This could guide the design of quantum simulators and information processing devices where scrambling must be controlled (harnessed or suppressed).

Our LE calculations for perturbed systems without hilltops also show small amplitude oscillations in all the chosen models. This aligns with our observations of OTOCs.

The general observation is that the specific characteristics of OTOCs occur whenever the slope in the potential has a positive minimum. This naturally includes symmetric potential having a clear hilltop.

Author contributions

All authors contributed equally to this manuscript. All author have read and approved the final version of the manuscript.

Data Availability Statement The data supporting the findings of this study are available from the corresponding author upon reasonable request. Access will be granted in compliance with applicable ethical and legal guidelines.

Appendix A:

For a Hamiltonian of form Eq. (3), we have

$$\left[\hat{\mathcal{H}}, \hat{x}\right] = -2i\hat{p}. \tag{A1}$$

Applying $\langle m |...| n\rangle$ to the both sides of the equation, we obtain

$$\begin{aligned}
\left\langle m \left| \left[\hat{\mathcal{H}}, \hat{x}\right] \right| n \right\rangle &= -2i \langle m |\hat{p}| n\rangle = -2ip_{mn} \\
\Rightarrow -2ip_{mn} &= \left\langle m \left| \left[\hat{\mathcal{H}}, \hat{x}\right] \right| n \right\rangle \\
&= \left\langle m \left| \hat{\mathcal{H}}\hat{x} \right| n \right\rangle - \left\langle m \left| \hat{x}\hat{\mathcal{H}} \right| n \right\rangle \\
&= E_m \langle m |\hat{x}| n\rangle - E_n \langle m |\hat{x}| n\rangle, \\
&\qquad (\because \hat{\mathcal{H}}^\dagger = \hat{\mathcal{H}} \;\&\; \hat{\mathcal{H}}|m\rangle = E_m|m\rangle) \\
&= (E_m - E_n) \langle m |\hat{x}| n\rangle \\
&= E_{mn}x_{mn} \\
\Rightarrow p_{mn} &= \frac{i}{2}E_{mn}x_{mn} \qquad \text{(A2)}
\end{aligned}$$

Appendix B: Energy eigenvalue vs width of the potential (L)

Figure 13 shows that eigenvalues are independent of the width L beyond a critical value, L_c. In actual calculation, we choose $L > L_c$.

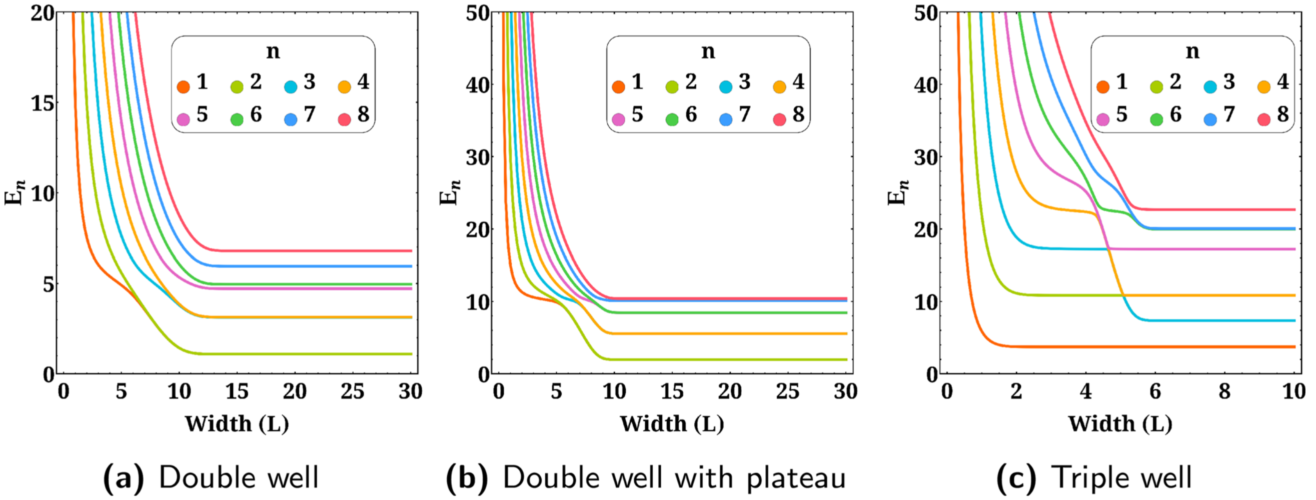

(a) Double well **(b)** Double well with plateau **(c)** Triple well

Fig. 13 First 8 energy eigenvalues as a function of the position of the width of the potential (L) for the three Models with $\sigma = 0$. Similar results are also found for rest of the cases. Note that as L increases, energy decreases non-monotonically

References

1. A. Wolf, J.B. Swift, H.L. Swinney, J.A. Vastano, Determining lyapunov exponents from a time series. Physica D: Nonlinear Phenomena **16**(3), 285–317 (1985)
2. M.-F. Danca, N. Kuznetsov, Matlab code for lyapunov exponents of fractional-order systems. Int. J. Bifurcat. Chaos. **28**(05), 1850067 (2018)
3. F. Christiansen, H.H. Rugh, Computing lyapunov spectra with continuous gram - schmidt orthonormalization. Nonlinearity **10**, 1063 (1997)
4. S. Habib, R.D. Ryne, Symplectic calculation of lyapunov exponents. Phys. Rev. Lett. **74**, 70–73 (1995)
5. O. Bohigas, M.J. Giannoni, C. Schmit, Characterization of chaotic quantum spectra and universality of level fluctuation laws. Phys. Rev. Lett. **52**, 1–4 (1984)
6. F. Haake, S. Gnutzmann, M. Kuś, *Quantum Signatures of Chaos. Springer Series in Synergetics* (Springer International Publishing, 2019)
7. J.S. Cotler, G. Gur-Ari, M. Hanada, J. Polchinski, P. Saad, S.H. Shenker, A. Stanford, Douglasand Streicher, M. Tezuka, Black holes and random matrices. J. High Energy Phys. **2017**, 118 (2017)
8. A. Gaikwad, R. Sinha, Spectral form factor in non-gaussian random matrix theories. Phys. Rev. D **100**, 026017 (2019)
9. J. Liu, Spectral form factors and late time quantum chaos. Phys. Rev. D **98**, 086026 (2018)
10. T. Guhr, A. Müller-Groeling, H.A. Weidenmüller, Random-matrix theories in quantum physics: common concepts. Phys. Rep. **299**(4), 189–425 (1998)
11. X. Wang, S. Ghose, B.C. Sanders, B. Hu, Entanglement as a signature of quantum chaos. Phys. Rev. E **70**, 016217 (2004)
12. P. Zanardi, C. Zalka, L. Faoro, Entangling power of quantum evolutions. Phys. Rev. A **62**, 030301 (2000)
13. A. Lakshminarayan, Entangling power of quantized chaotic systems. Phys. Rev. E **64**, 036207 (2001)
14. P. Zanardi, Entanglement of quantum evolutions. Phys. Rev. A **63**, 040304 (2001)
15. N. Anand, G. Styliaris, M. Kumari, P. Zanardi, Quantum coherence as a signature of chaos. Phys. Rev. Res. **3**, 023214 (2021)
16. A. Peres, Stability of quantum motion in chaotic and regular systems. Phys. Rev. A **30**, 1610–1615 (1984)
17. R.A. Jalabert, H.M. Pastawski, Environment-independent decoherence rate in classically chaotic systems. Phys. Rev. Lett. **86**, 2490–2493 (2001)
18. P. Jacquod, Semiclassical time evolution of the reduced density matrix and dynamically assisted generation of entanglement for bipartite quantum systems. Phys. Rev. Lett. **92**, 150403 (2004)
19. C. Petitjean, P. Jacquod, Lyapunov generation of entanglement and the correspondence principle. Phys. Rev. Lett. **97**, 194103 (2006)
20. P. Jacquod, C. Petitjean, Decoherence, entanglement and irreversibility in quantum dynamical systems with few degrees of freedom. Adv. Phys. **58**(2), 67–196 (2009)
21. I. García-Mata, M. Saraceno, R.A. Jalabert, A.J. Roncaglia, D.A. Wisniacki, Chaos signatures in the short and long time behavior of the out-of-time ordered correlator. Phys. Rev. Lett. **121**, 210601 (2018)
22. R. N. Das, S. Dutta, A. Maji, "Generalised out-of-time-order correlator in supersymmetric quantum mechanics," (2022)
23. P. Zanardi, N. Anand, Information scrambling and chaos in open quantum systems. Phys. Rev. A **103**, 062214 (2021)
24. P. Romatschke, Quantum mechanical out-of-time-ordered-correlators for the anharmonic (quartic) oscillator. J. High Energy Phys. **2021**, 30 (2021)
25. M.A. Prado Reynoso, G.J. Delben, M. Schlesinger, M.W. Beims, Finite-time Lyapunov fluctuations and the upper bound of classical and quantum out-of-time-ordered expansion rate exponents. Phys. Rev. E. **106**(6), L062201 (2022)
26. R.J. Lewis-Swan, A. Safavi-Naini, J.J. Bollinger, A.M. Rey, Unifying scrambling, thermalization and entanglement through measurement of fidelity out-of-time-

order correlators in the dicke model. Nat. Commun. **10**, 1581 (2019)
27. R.J. Garcia, Y. Zhou, A. Jaffe, Quantum scrambling with classical shadows. Phys. Rev. Res. **3**, 033155 (2021)
28. A. Lakshminarayan, Out-of-time-ordered correlator in the quantum bakers map and truncated unitary matrices. Phys. Rev. E **99**, 012201 (2019)
29. E.B. Rozenbaum, S. Ganeshan, V. Galitski, Lyapunov exponent and out-of-time-ordered correlator's growth rate in a chaotic system. Phys. Rev. Lett. **118**, 086801 (2017)
30. F. Meier, M. Steinhuber, J.D. Urbina, D. Waltner, T. Guhr, Signatures of the interplay between chaos and local criticality on the dynamics of scrambling in many-body systems. Phys. Rev. E **107**, 054202 (2023)
31. T. Ali, A. Bhattacharyya, S.S. Haque, E.H. Kim, N. Moynihan, J. Murugan, Chaos and complexity in quantum mechanics. Phys. Rev. D **101**, 026021 (2020)
32. I. Kukuljan, S.. c. v. Grozdanov, T.. c. v. Prosen, Weak quantum chaos. Phys. Rev. B **96**, 060301 (2017)
33. E.M. Fortes, I. García-Mata, R.A. Jalabert, D.A. Wisniacki, Gauging classical and quantum integrability through out-of-time-ordered correlators. Phys. Rev. E **100**, 042201 (2019)
34. A.I. Larkin, Y.N. Ovchinnikov, Quasiclassical method in the theory of superconductivity. Soviet J. Exp. Theoret. Phys. **28**, 1200 (1969)
35. S. Sinha, S. Ray, S. Sinha, Classical route to ergodicity and scarring in collective quantum systems. J. Phys.: Condens. Matter **36**, 163001 (2024)
36. K. Hashimoto, K.-B. Huh, K.-Y. Kim, R. Watanabe, Exponential growth of out-of-time-order correlator without chaos: inverted harmonic oscillator. J. High Energy Phys. **2020**, 68 (2020)
37. R.A. Kidd, A. Safavi-Naini, J.F. Corney, Saddle-point scrambling without thermalization. Phys. Rev. A **103**, 033304 (2021)
38. B. Bhattacharjee, X. Cao, P. Nandy, T. Pathak, Krylov complexity in saddle-dominated scrambling. J. High Energy Phys. **2022**(5), 1–27 (2022)
39. W. Kirkby, D.H.J. O'Dell, J. Mumford, False signals of chaos from quantum probes. Phys. Rev. A **104**, 043308 (2021)
40. T. Xu, T. Scaffidi, X. Cao, Does scrambling equal chaos? Phys. Rev. Lett. **124**, 140602 (2020)
41. T. Morita, Extracting classical lyapunov exponent from one-dimensional quantum mechanics. Phys. Rev. D **106**, 106001 (2022)
42. K. Hashimoto, K. Murata, R. Yoshii, Out-of-time-order correlators in quantum mechanics. J. High Energy Phys. **2017**, 138 (2017)
43. P. Garbaczewski, V.A. Stephanovich, G. Engel, Electron spectra in double quantum wells of different shapes. New J. Phys. **24**, 033052 (2022)
44. N. Aquino, J. Garza, G. Campoy, A. Vela, Energy eigenvalues for free and confined triple-well potentials. Rev. Mex. Fis. **57**, 46–52 (2011)
45. K.W. Wittmann, E.R. Castro, A. Foerster, L.. F.. Santos, Interacting bosons in a triple well: preface of many-body quantum chaos. Phys. Rev. E **105**, 034204 (2022)
46. R.J. Damburg, R.K. Propin, Y.I. Ryabykh, Perturbation theory for the triple-well anharmonic oscillator. Phys. Rev. A **41**, 1218–1224 (1990)
47. L. N. Hand and J. D. Finch, "Chaotic dynamics," in Analytical Mechanics, p. 423–492, Cambridge University Press, (1998)
48. L. Reichl, "Bounded quantum systems," in The Transition to Chaos: Conservative Classical and Quantum Systems, pp. 195–237, Cham: Springer International Publishing, (2021)
49. P. Bracken, "Introductory chapter: Dynamical symmetries and quantum chaos," in Research Advances in Chaos Theory (P. Bracken, ed.), ch. 1, Rijeka: IntechOpen, (2020)
50. W.-M. Zhang, D.H. Feng, J.-M. Yuan, S.-J. Wang, Integrability and nonintegrability of quantum systems: Quantum integrability and dynamical symmetry. Phys. Rev. A **40**, 438–447 (1989)
51. G.-H. Sun, Q. Dong, V.B. Bezerra, S.-H. Dong, Exact solutions of an asymmetric double well potential. J. Math. Chem. **60**, 605–612 (2022)
52. G. Theocharis, P.G. Kevrekidis, D.J. Frantzeskakis, P. Schmelcher, Symmetry breaking in symmetric and asymmetric double-well potentials. Phys. Rev. E **74**, 056608 (2006)
53. Y. Nambu, "Dynamical symmetry breaking," in Broken Symmetry, pp. 436–451, (1995)
54. S. Sarkar, J.S. Satchell, Quantum chaos in the Lorenz equations with symmetry breaking. Phys. Rev. A **35**, 398–405 (1987)
55. J. Song, B.A. Malomed, Z. Yan, Symmetry-breaking bifurcations and excitations of solitons in linearly coupled NLS equations with PT-symmetric potentials. Proc. R. Soc. A. **479**(2278), 20230457 (2023)
56. M. Field and M. Golubitsky, Symmetry in Chaos: A Search for Pattern in Mathematics, Art and Nature, Second Edition. Other Titles in Applied Mathematics, Society for Industrial and Applied Mathematics, (2009)
57. A. Bayliss, B.J. Matkowsky, *Bifurcation, pattern formation and chaos in combustion* (Springer, 1991)
58. A.L. Krause, E.A. Gaffney, T.J. Jewell, V. Klika, B.J. Walker, Turing instabilities are not enough to ensure pattern formation. Bull. Math. Biol. **86**(2), 21 (2024)
59. P. Chossat, M. Golubitsky, Symmetry-increasing bifurcation of chaotic attractors. Physica D **32**(3), 423–436 (1988)
60. K.G. Szabó, T. Tél, On the symmetry-breaking bifurcation of chaotic attractors. J. Stat. Phys. **54**, 925–948 (1989)
61. R.A. Jalabert, I. García-Mata, D.A. Wisniacki, Semiclassical theory of out-of-time-order correlators for low-dimensional classically chaotic systems. Phys. Rev. E **98**, 062218 (2018)
62. J.S. Cotler, D. Ding, G.R. Penington, Out-of-time-order operators and the butterfly effect. Ann. Phys. **396**, 318–333 (2018)
63. S.S. Haque, B. Underwood, Squeezed out-of-time-order correlator and cosmology. Phys. Rev. D **103**, 023533 (2021)
64. K.Y. Bhagat, B. Bose, S. Choudhury, S. Chowdhury, R.N. Das, S.G. Dastider, N. Gupta, A. Maji, G.D. Pasquino, S. Paul, The generalized OTOC from supersymmetric quantum mechanics—study of random fluc-

tuations from eigenstate representation of correlation functions. Symmetry **13**(1), 44 (2020)

65. I. García-Mata, R.A. Jalabert, D.A. Wisniacki, Out-of-time-order correlations and quantum chaos. Scholarpedia **18**(4), 55237 (2023)
66. J. Chávez-Carlos, B. López-del Carpio, M.A. Bastarrachea-Magnani, P. Stránský, S. Lerma-Hernández, L.F. Santos, J.G. Hirsch, Quantum and classical lyapunov exponents in atom-field interaction systems'. Phys. Rev. Lett. **122**, 024101 (2019)
67. E.B. Rozenbaum, S. Ganeshan, V. Galitski, Universal level statistics of the out-of-time-ordered operator. Phys. Rev. B **100**, 035112 (2019)
68. R.K. Shukla, A. Lakshminarayan, S.K. Mishra, Out-of-time-order correlators of nonlocal block-spin and random observables in integrable and nonintegrable spin chains. Phys. Rev. B **105**, 224307 (2022)
69. J. Maldacena, S.H. Shenker, D. Stanford, A bound on chaos. J. High Energy Phys. **2016**, 106 (2016)
70. M. Zonnios, J. Levinsen, M.M. Parish, F.A. Pollock, K. Modi, Signatures of quantum chaos in an out-of-time-order tensor. Phys. Rev. Lett. **128**, 150601 (2022)
71. T. Akutagawa, K. Hashimoto, T. Sasaki, and R. Watanabe, "Out-of-time-order correlator in coupled harmonic oscillators," Journal of High Energy Physics, vol. 2020, Aug 2020
72. A. Bhattacharyya, W. Chemissany, S.S. Haque, B. Yan, Towards the web of quantum chaos diagnostics. Europ. Phys. J. C **82**(1), 87 (2022)
73. A. Masoumi, F. Pellicano, F.S. Samani, M. Barbieri, Symmetry breaking and chaos-induced imbalance in planetary gears. Nonlinear Dyn. **80**, 561–582 (2015)
74. A. Bhattacharyya, W. Chemissany, S.S. Haque, J. Murugan, B. Yan, The multi-faceted inverted harmonic oscillator: Chaos and complexity. SciPost Phys. Core **4**, 002 (2021)
75. S. Gentilini, M.C. Braidotti, G. Marcucci, E. DelRe, C. Conti, Physical realization of the glauber quantum oscillator. Sci. Rep. **5**, 15816 (2015)
76. V. Subramanyan, S.S. Hegde, S. Vishveshwara, B. Bradlyn, Physics of the inverted harmonic oscillator: from the lowest landau level to event horizons. Ann. Phys. **435**, 168470 (2021)
77. S. Choudhury, S.P. Selvam, K. Shirish, Circuit complexity from supersymmetric quantum field theory with morse function. Symmetry **14**, 1656 (2022)
78. Z.-M. Xu, B. Wu, W.-L. Yang, van der waals fluid and charged ads black hole in the landau theory. Class. Quant. Gravit. **38**, 205008 (2021)
79. R. Li, J. Wang, Generalized free energy landscape of a black hole phase transition. Phys. Rev. D **106**, 106015 (2022)
80. S.-W. Wei, Y.-X. Liu, Y.-Q. Wang, Dynamic properties of thermodynamic phase transition for five-dimensional neutral gauss-bonnet ads black hole on free energy landscape. Nucl. Phys. B **976**, 115692 (2022)
81. Y.-Z. Du, H.-F. Li, F. Liu, L.-C. Zhang, Dynamic property of phase transition for non-linear charged anti-de sitter black holes *. Chin. Phys. C **46**, 055104 (2022)
82. V. I. Kuvshinov, A. V. Kuzmin, and V. A. Piatrou, "Asymmetric double well system as effective model for the kicked one," 2011
83. R.P. McRae, B.C. Garrett, Anharmonic corrections to variational transition state theory calculations of rate constants for a model activated reaction in solution. J. Chem. Phys. **98**, 6929–6934 (1993)
84. A.J. Brizard, M.C. Westland, Motion in an asymmetric double well. Commun. Nonlinear Sci. Numer. Simul. **43**, 351–368 (2017)
85. M. Selg, Exactly solvable asymmetric double-well potentials. Phys. Scr. **62**, 108 (2000)
86. S.H. Strogatz, *Bifurcation, in nonlinear dynamics and chaos: with applications to physics* (Chemistry and Engineering, Westview Press, Biology, 2000)
87. G. Gaeta, Bifurcation and symmetry breaking. Phys. Rep. **189**(1), 1–87 (1990)
88. D.A. Zezyulin, M.E. Lebedev, G.L. Alfimov, B.A. Malomed, Symmetry breaking in competing single-well linear-nonlinear potentials. Phys. Rev. E **98**, 042209 (2018)
89. R.J.W. Hodgson, Y.P. Varshni, Splitting in a double-minimum potential with almost twofold degenerate lower levels. J. Phys. A: Math. Gen. **22**, 61 (1989)
90. N. Gupta, A.K. Roy, B.M. Deb, One-dimensional multiple-well oscillators: A time-dependent quantum mechanical approach. Pramana **59**, 575–583 (2002)
91. J. J. Sakurai and J. Napolitano, "Symmetry in quantum mechanics," in Modern Quantum Mechanics, p. 262–302, Cambridge University Press, 2 ed., 2017
92. O. Vallée and M. Soares, Airy Functions and Applications to Physics. IMPERIAL COLLEGE PRESS, 2004
93. M. Abramowitz, I. Stegun, *Handbook of mathematical functions: with formulas, graphs, and mathematical tables* (Dover Books on Mathematics, Dover Publications, 2012)
94. A. Landau, Y. Aharonov, E. Cohen, Realization of qudits in coupled potential wells. Int. J. Quant. Inform. **14**(05), 1650029 (2016)
95. J.M. Taylor, V. Srinivasa, J. Medford, Electrically protected resonant exchange qubits in triple quantum dots. Phys. Rev. Lett. **111**, 050502 (2013)
96. M.V. Suslov, G.B. Lesovik, G. Blatter, Quantum abacus for counting and factorizing numbers. Phys. Rev. A **83**, 052317 (2011)
97. G. McCormack, R. Nath, W. Li, Nonlinear dynamics of rydberg-dressed bose-einstein condensates in a triple-well potential. Phys. Rev. A **102**, 063329 (2020)
98. E. Castro, J. Chávez-Carlos, I. Roditi, L.F. Santos, J.G. Hirsch, Quantum-classical correspondence of a system of interacting bosons in a triple-well potential. Quantum **5**, 563 (2021)
99. W.-T. Lu, S.-J. Wang, Property of quantum tunneling in a driven triple-well potential. Chem. Phys. **368**(1), 93–99 (2010)
100. J. Casahorrán, Analysis of non-perturbative fluctuations in a triple-well potential. Phys. Lett. A **283**(5), 285–290 (2001)
101. P. Romatschke, Out-of-time-ordered-correlators for the pure inverted quartic oscillator: classical chaos meets quantum stability. J. High Energy Phys. **2024**(10), 1–17 (2024)
102. A. Chenu, I.L. Egusquiza, J. Molina-Vilaplana, A. del Campo, Quantum work statistics, loschmidt echo and information scrambling. Sci. Rep. **8**, 12634 (2018)

103. A. Goussev, R.A. Jalabert, H.M. Pastawski, D.A. Wisniacki, Loschmidt echo. Scholarpedia **7**(8), 11687 (2012)
104. T. Gorin, T. Prosen, T.H. Seligman, M. Žnidaric, Dynamics of loschmidt echoes and fidelity decay. Phys. Rep. **435**(2), 33–156 (2006)
105. B. Yan, L. Cincio, W.H. Zurek, Information scrambling and loschmidt echo. Phys. Rev. Lett. **124**, 160603 (2020)
106. M. Serbyn, D.A. Abanin, Loschmidt echo in many-body localized phases. Phys. Rev. B **96**, 014202 (2017)
107. S. Pg, V. Madhok, A. Lakshminarayan, Out-of-time-ordered correlators and the loschmidt echo in the quantum kicked top: how low can we go? J. Phys. D Appl. Phys. **54**, 274004 (2021)
108. C.M. Sánchez, A.K. Chattah, K.X. Wei, L. Buljubasich, P. Cappellaro, H.M. Pastawski, Perturbation independent decay of the loschmidt echo in a many-body system. Phys. Rev. Lett. **124**, 030601 (2020)
109. P. Jacquod, I. Adagideli, C.W.J. Beenakker, Anomalous power law of quantum reversibility for classically regular dynamics. Europhys. Lett. **61**, 729 (2003)
110. A. Wisniacki, Loschmidt echo. Scholarpedia **7**(8), 11687 (2012)
111. P. Jacquod, P. Silvestrov, C. Beenakker, Golden rule decay versus lyapunov decay of the quantum loschmidt echo. Phys. Rev. E **64**, 055203 (2001)
112. N.R. Cerruti, S. Tomsovic, A uniform approximation for the fidelity in chaotic systems. J. Phys. A: Math. Gen. **36**, 11915 (2003)
113. T. Prosen, M. Znidaric, Stability of quantum motion and correlation decay. J. Phys. A: Math. Gen. **35**, 1455 (2002)